055

THE ONSET OF DYNAMIC STALL: A TIME-RESOLVED APPROACH

KAREN MULLENERS AND MARKUS RAFFEL

German Aerospace Center (DLR) – Institute of Aerodynamics and Flow Technology
Bunsenstr. 10, 37073 Göttingen, Germany

Abstract The flow over an oscillating OA209 airfoil under dynamic stall conditions was investigated by means of unsteady surface pressure measurements and time-resolved particle image velocimetry. The characteristic features of the unsteady flow field were identified and analysed utilising different coherent structure identification methods. An Eulerian and a Lagrangian procedure were adopted to locate the axes of vortices and the edges of Lagrangian coherent structures, respectively. The complementary information obtained by these methods provided deeper insight into the spatiotemporal evolution of vortical structures within a single dynamic stall life cycle. In particular, the physical mechanisms heralding the formation of the primary dynamic stall vortex were identified as the emergence and subsequent roll up of a shear layer at the interface between the free stream and the reversing flow near the airfoils surface. Accordingly, the stall development was subdivided into two parts: a primary instability stage followed by a secondary instability or vortex formation stage. The characteristic time scales associated with the first stage revealed an overall decrease of the dynamic stall delay with increasing unsteadiness. The delay attributed to the vortex formation stage was observed to be unaffected by variations in the airfoils dynamics. The combination of time-resolved imaging and extensive coherent structure analysis was shown to provide a new approach to different aspects of dynamic stall.

1 INTRODUCTION

The dynamic stall process of an airfoil comprises a series of complex aerodynamic phenomena in response to an unsteady change of the angle of attack. It is accompanied by a lift overshoot and delayed massive flow separation with respect to static stall. The salient feature of the unsteadily separating flow is the formation and convection of a large-scale coherent structure referred to as the dynamic stall vortex. The most prominent example can be observed on the retreating blades of an helicopter rotor in forward flight. Although the dynamic stall delay and the related increase of the maximum lift can be beneficial in some applications, the large excursions of the aerodynamic loads that emerge during vortex break down induce strong vibrations and structural loads, potentially fatal for a helicopter rotor. Hence, due to the incessant interest in improving the manoeuvrability and performance of rotary-wing aircraft and rapidly manoeuvring aircraft, dynamic stall has been and still remains the subject of vivid interest [11, 21, 20].

A detailed analysis of the dynamic stall events on an oscillating airfoil was presented by Carr et al. [1]. They revealed that the prominent features within a full cycle of oscillation are consecutively: the emergence and spreading of flow reversal on the airfoil's suction side, the formation and convection of a large-scale leading edge vortex, massive flow separation, and finally flow reattachment. Analogously, Shih et al. [19] classified the unsteady flow development over an airfoil pitching up at constant rate into four successive stages: 1) a vortex formation stage, 2) a vortex convection stage, 3) stall onset, and 4) a stalled stage. Both descriptions show that the flow over either a constantly pitching or oscillating airfoil is qualitatively characterised by the same prominent features, being the initiation, growth and shedding of a leading edge vortex and the associated lift overshoot. For both types of motion the process of vortex formation and convection result in a delay of massive flow separation to angles of attack beyond the static stall angle. During this delay the lift continues to increase with increasing angle of attack yielding the lift overshoot which is characteristic of dynamic stall. The inception of stall is generally accompanied by a loss of lift and an increase of the negative pitching moment

and marks the beginning of the stalled stage. This stage can be recognised by large-scale vortex shedding and associated large fluctuations of the lift, drag and pitching moment. Furthermore, when the airfoil motion is oscillatory, a large amount of load hysteresis is present.

Although a lot of effort – analytical as well as numerical and experimental – has been devoted in the past to enhance the comprehension of the phenomenology of dynamic stall, it is not yet fully understood and characterised. In particular, the process that leads to the formation of the primary stall vortex and the mechanism that causes the vortex to break contact with the airfoil are still controversial issues requiring further and deeper examination.

Accurate knowledge of the state of the fluid flow during dynamic stall is strongly tied to a fundamental understanding of the development and interaction of coherent structures. Due to the incessant technological progress during the last decades yielding the development of state-of-the-art digital cameras, high repetition rate lasers and sophisticated evaluation algorithms, the particle image velocimetry (PIV) technique established itself as a valuable and indispensable tool in experimental fluid dynamics. However, the investigation of vortices and vortex dynamics from experimental data remains a challenging task due to the lack of a universally accepted definition of vortical structures and the difficulty to quantify them. Several specific definitions have been proposed hitherto, i. a. [10, 6]. Despite the plethora of publications on the issue no consensus has been reached yet, reflecting the complexity of the subject area. As a direct consequence, unambiguous vortex detection remains elusive and various Eulerian and Lagrangian criteria have been introduced over the years with different validity depending on the specific problem.

Within the scope of this study, the conspicuous features of the experimentally investigated flow over a sinusoidally oscillating airfoil in a uniform flow are identified and analysed utilising a combination of an Eulerian vortex centre allocation procedure [13] and a Lagrangian approach based on the Lyapunov exponent [7]. Whereas past experimental investigations generally involve phase-locked measurements, the present study provides time-resolved recordings of the velocity field in addition to unsteady airfoil's surface pressure distributions and allows for the examination of the chronology of events leading to the onset of dynamic stall.

The onset of stall under dynamic conditions is generally defined as the detachment of the primary stall vortex and was specified earlier in the present context by Mulleners and Raffel [14] based on a characteristic mode of the proper orthogonal decomposition (POD) of the velocity field. Variations in the flow field topology that accompany the stall onset were verified by a Lagrangian coherent structure analysis. Furthermore, a subtle but significant change was observed in the orientation of the trajectories of the vortices that originate at the very leading edge shortly before and after stall onset. Due to the congruence with the Eulerian and Lagrangian picture shown in Mulleners and Raffel [14], the POD-based assignment of the stall onset is deemed to be reliable and was utilised to specify the dynamic stall onset for the present parameter combinations.

The next logical step – and the main focus of this paper – is to assess the associated time delay with respect to static stall. Furthermore, in order to model and predict the dynamic stall onset and delay, special emphasis is placed on the identification and characterisation of the physical mechanisms and parameters that play a key role in the initiation, growth, and subsequent detachment of the dynamic stall vortex.

The paper is organised as follows. Prior to the description of the applied coherent structure identification procedures, the experimental details will be specified. Subsequently, the experimental results are presented and discussed. The discussion covers the examination of the chronology of events heralding stall onset and a detailed analysis of the associated time-scales. The discussion is concluded by a short summary of the most important findings and by suggesting further avenues of investigation.

2 EXPERIMENTAL SET-UP

Wind tunnel experiments were conducted to investigate dynamic stall on a constantly pitching airfoil in a uniform flow at a free stream Reynolds number $Re = 9.2 \times 10^5$ based on the chord length c, with $c = 0.3\,m$ (Mach number $Ma = 0.14$). A two-dimensional airfoil model with an OA209 profile was subjected to a sinusoidal oscillating motion about its quarter chord axis with a mean incidence α_0, an amplitude α_1, and an oscillation frequency f_{osc}. The latter is preferably written in dimensionless form as the reduced frequency $k = \pi f_{osc} c/U_\infty$, where U_∞ is the free steam velocity. The mean incidence, amplitude and reduced frequency were varied such that $\alpha_0 \in \{18°, 20°, 22°\}$, $\alpha_1 \in \{6°, 8°\}$, and $k \in \{0.050, 0.075, 0.10\}$.

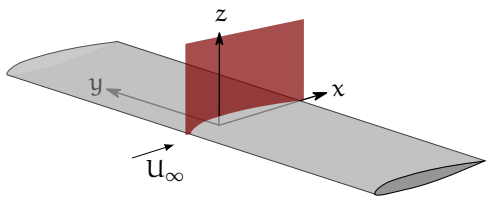

Figure 1: Position of the PIV field of view.

Stereoscopic time-resolved particle image velocity (TR-PIV) measurements were conducted in the cross sectional plane at model mid-span (see figure 1). The width of the field of view covered the entire chord for the relevant angle of attack range. As maximally allowed by the hardware, time series of 6144 frames with full camera resolution were recorded at 3000 Hz, corresponding to an acquisition rate of 1500 Hz for the velocity fields. After mapping the views of both cameras, the dimensions of the PIV measurement window were 335 mm × 165 mm and the spatial resolution of the recording was 5.0 px/mm. The PIV images were processed using an interrogation window size of 32 px × 32 px and an overlap of approximately 80 % yielding a grid spacing of 6 px or 1.2 mm which is less then 0.005 c. The interrogation window size was minimised ensuring an acceptable signal-to-noise ratio. The window overlap on the other hand was maximised to avoid artificial smoothing of velocity gradients [17]. By doing so the spatial resolution of the results of the vortex detection algorithms was improved. Prior to the coherent structure analysis, the velocity fields were rotated into the airfoil reference system with the x-axis along the chord, the y-axis along the span and the z-axis upward perpendicular to the chord. The origin coincides with the rotation axis, i. e. the airfoil's quarter chord axis, at model mid-span. Simultaneously to the TR-PIV, the surface pressure distribution at the model mid-span was scanned at approximately 6 kHz for about 15 s. The data acquisition was synchronised with the recording of the PIV images allowing for straightforward assignment of the instantaneous pressure distributions to each of the acquired velocity fields.

3 COHERENT STRUCTURE ANALYSIS

The common goal of coherent structure identification methods is to locate, extract, and visualise conspicuous flow structures characterised by various spatial and temporal scales. In the context of the present paper, two different methods to analyse coherent structure were adopted; one Eulerian and one Lagrangian procedure.

The Eulerian method utilises the dimensionless scalar function Γ that was first introduced by Michard et al. [13] to locate the axis of individual vortices. The function is derived directly from the two-dimensional in-plane velocity field and is defined in discrete form as

$$\begin{aligned}\Gamma(\mathbf{x}_i) &= \frac{1}{M}\sum_{\mathbf{x}_j \in S_i} \frac{\left[(\mathbf{x}_j-\mathbf{x}_i)\times(\mathbf{u}_j-\tilde{\mathbf{u}}_i)\right]\cdot\mathbf{n}}{|\mathbf{x}_j-\mathbf{x}_i|\cdot|\mathbf{u}_j-\tilde{\mathbf{u}}_i|} \\ &= \frac{1}{M}\sum_{\mathbf{x}_j \in S_i} \sin(\theta_{ij}) \quad ,\end{aligned} \tag{1}$$

with S_i a two-dimensional area around $\mathbf{x}_i$, M the number of grid points $\mathbf{x}_j$ inside S_i with $j \neq i$, $\mathbf{n}$ the unit normal vector, $\mathbf{u}_j$ the velocity at $\mathbf{x}_j$, $\tilde{\mathbf{u}}_i$ the local mean velocity around $\mathbf{x}_i$, and θ_{ij} the angle formed by the vectors $\mathbf{x}_j-\mathbf{x}_i$ and $\mathbf{u}_j-\tilde{\mathbf{u}}_i$. The local mean velocity is taken into account in order for Γ to be Galilean invariant (cf. [4]).

According to its definition, Γ is a dimensionless scalar function, with $-1 \leqslant \Gamma \leqslant 1$. The location of possible vortex axes is indicated by the local extrema of Γ and the sense of rotation is given by the sign of the local extremum. Besides the detection of the location of the vortex centres, their trajectories over a time series of flow fields have been traced. For this purpose, the convection velocity of the individual identified vortex centres within the reference frame are used to predict their future position and narrow the number of possible follow-up vortices.

The most popular Lagrangian approach, which was adopted in the present study, leverages finite-time Lyapunov exponents (FTLEs) and was introduced by Haller and Yuan [7]. The FTLE method reverts directly to the fluid particle trajectories and is therefore inherently objective, includes information on the history of the flow, and has a clear physical interpretation. The particle trajectories can be integrated in forward as well as in backward time yielding positive finite-time Lyapunov exponent (pFLTE) and negative finite-time Lyapunov exponent (nFTLE) fields. The ridges in the pFTLE field reveal material lines normal to which fluid particles are being stretched or repelled, consequentially they are referred to as repelling material lines or stable manifolds. Vice versa, ridges in nFTLE fields visualise attracting materials or unstable manifolds, i. e. lines along which fluid particles are being elongated, when integrating the trajectories in backward time. The flow field around the intersection of a repelling and an attracting material line resembles that of a saddle point. Moreover, when attached to a solid surface attracting material lines depict separation lines while attachment lines are repelling material lines. This FTLE method thus yields candidate material lines and captures features of the flow that are familiar from flow visualisation experiments. According to Shadden et al. [18] the ridges in the FTLE fields delineate regions that exhibit qualitatively different dynamical behaviour, hence indicated the boundaries of Lagrangian coherent structures (LCSs). For a comprehensive discussion of the general properties and basic concepts involved in the computation of the FTLE, the reader is referred to i. a. [5, 3].

The combination of two vortex identification procedures that are different in nature allows for different aspects of the flow to be highlighted and delivers a more detailed insight into the vortex dynamics.

4 RESULTS AND DISCUSION

Analogous to the classification of Shih et al. [19] with regard to the flow over an airfoil pitching-up at constant rate, the unsteady flow development over an oscillation airfoil can be divided into five different stages [14]. With the starting point of a cycle taken at the minimum incidence angle, the flow will consecutively pass through the following stages within each individual cycle: 1) the *attached flow stage*; 2) the *stall development stage*; 3) *stall onset*; 4) the *stalled stage*; and 5) *flow reattachment*. The onset of dynamic stall, defined as the detachment of the primary stall vortex, was specified for the available time resolved velocity field data based on a characteristic POD mode as reported in a preceding publication (see [14]). The focus in the present paper lies on the analysis of the peculiarities of the dynamic stall development, including the succession of the physical mechanisms that herald stall onset, the governing parameters, and the relevant time-scales.

4.1 *Triggering Mechanism*

The dynamic stall process is deemed to be an interesting example of unsteady separation. It is initiated by an adverse pressure gradient and involves a recirculation region originating within the region of this local adverse gradient. The observations presented in [14] revealed a prominent recirculation zone on the airfoil's suction side which grows in a direction normal to the surface when the airfoil pitches up. This is analogous to the basic mechanism heralding unsteady separation in the low-Reynolds-number regime described by Obabko and Cassel [15]. Furthermore, the shear layer that develops at the interface between this region of reversed flow and the free stream flow seems to play a major role in the stall development (cf. Ho [8]).

Based on the size of the region of flow reversal and the level of interaction between the shear layer vortices, the stall development stage can be subdivided into two parts. A first part essentially covers the growth of the recirculation region and the corresponding initial development of the free shear layer. This includes the emergence of individual shear layer vortices as a result of a primary instability. These small-scale vortices interact only weakly with each other while being convected downstream by the external flow. Inspired by the standard notions used to describe the evolution of a mixing layer (cf. [2]), this part of the stall development phase is termed the *primary instability stage*. Accordingly, the second part which is characterised by a secondary instability eliciting the free shear layer to roll up and form a large-scale dynamic stall vortex is termed the *secondary instability stage* or alternatively the *vortex formation stage*.

Prior to focussing on the two stages and their governing parameters individually, the transition between them is identified based on the temporal evolution of the average height of the shear layer, which is equivalent to the average height of the recirculation region. The latter is given by the average normal distance of the shear layer vortices with respect to the airfoil's upper surface. More general, the average height of all clockwise rotating vortical structures detected in an instantaneous experimental velocity field denoted by Δz

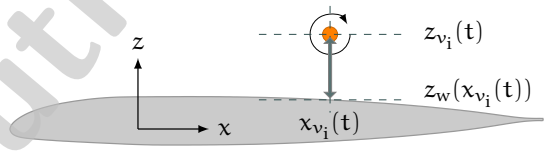

Figure 2: Definition of the ingredients required for the computation of Δz.

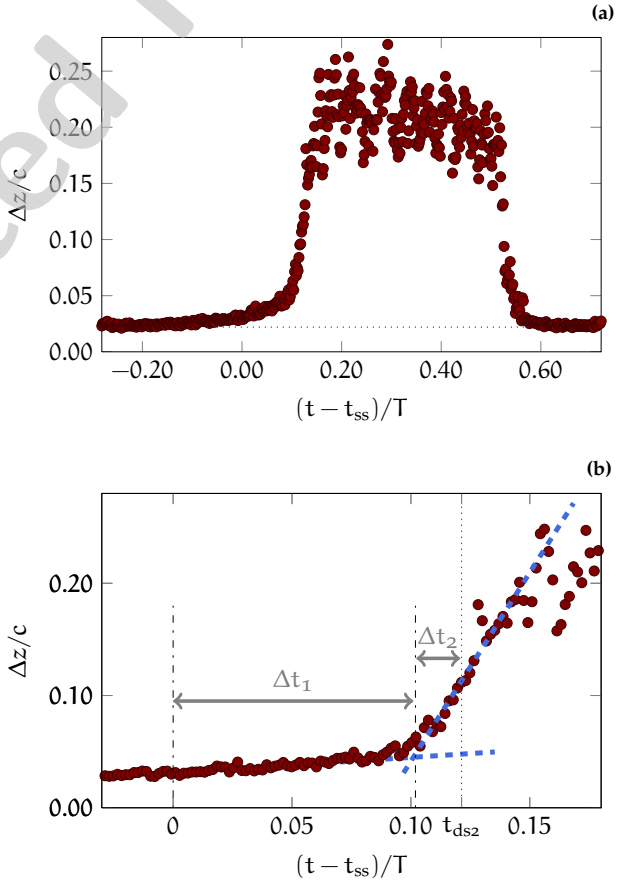

Figure 3: Evolution of the average vertical distance of the vortex cores from the airfoil's upper surface over one period (a) and in detail (b) with the corresponding linear fits. The horizontal and vertical, dotted lines indicate respectively the noise level due to experimental limitations and the specified onset of dynamic stall ($\alpha_o = 20°$, $\alpha_1 = 8°$, $k = 0.05$).

is calculated according to

$$\Delta z(t) = \frac{1}{N(t)} \sum_{i=1}^{N(t)} \left| z_{v_i}(t) - z_w(x_{v_i}(t)) \right| \quad , \qquad (2)$$

where $N(t)$ is the total number of clockwise rotating vortices detected in the instantaneous velocity field at time t using the Eulerian vortex detection algorithm, and where $\left| z_{v_i}(t) - z_w(x_{v_i}(t)) \right|$ is the normal distance of the individual vortices to the airfoil's upper surface as illustrated in figure 2. The average vortex height is calculated for all instantaneous velocity fields even when the vortices considered are not arranged in the shear layer and Δz can not be interpreted as the average shear layer height. A typical temporal evolution of Δz, normalised by c, for one oscillation period, T, is depicted in figure 3 for the dynamic stall case with $\alpha_0 = 20°$, $\alpha_1 = 8°$, and $k = 0.05$. Here, the values on the abscissa show the time lag with respect to the instant when the angle of attack exceeds the static stall angle, t_{ss}.

For small angles of attack, vorticity is a priori confined to the thin boundary layer and its transport is dominated by convection. Vorticity lumped into separate vortices is convected downstream along the airfoil's contour preventing the boundary layer from growing beyond a certain thickness. Hence, as long as the flow is fully attached the average height Δz is expected to be of the order of the boundary layer thickness. However, due to experimental limitations valid velocity information was only available down to approximately 2 mm above the airfoil's surface. Consequentially, minimum values of Δz for low angles of attack are erroneous and misleading. The horizontal, dotted line in figure 3(a) marks the minimum level of Δz corresponding to a fully attached flow.

With increasing angle of attack, the strongly accelerated flow around the leading edge is accompanied by a large pressure gradient which leads to an increased production of vorticity. Immediately downstream of the leading edge the flow decelerates, i. e. a local adverse streamwise pressure gradient emerges, as a result of which a recirculation zone develops there. The emergence and subsequent growth of the region of flow reversal can be readily understood from a vorticity point of view.

The vorticity distribution is initially confined to a small vortex sheet near the airfoil's surface which can be represented by a discrete train of two-dimensional point vortices. According to the vortex image pair analysis of Reynolds and Carr [16], mirror vortices – included

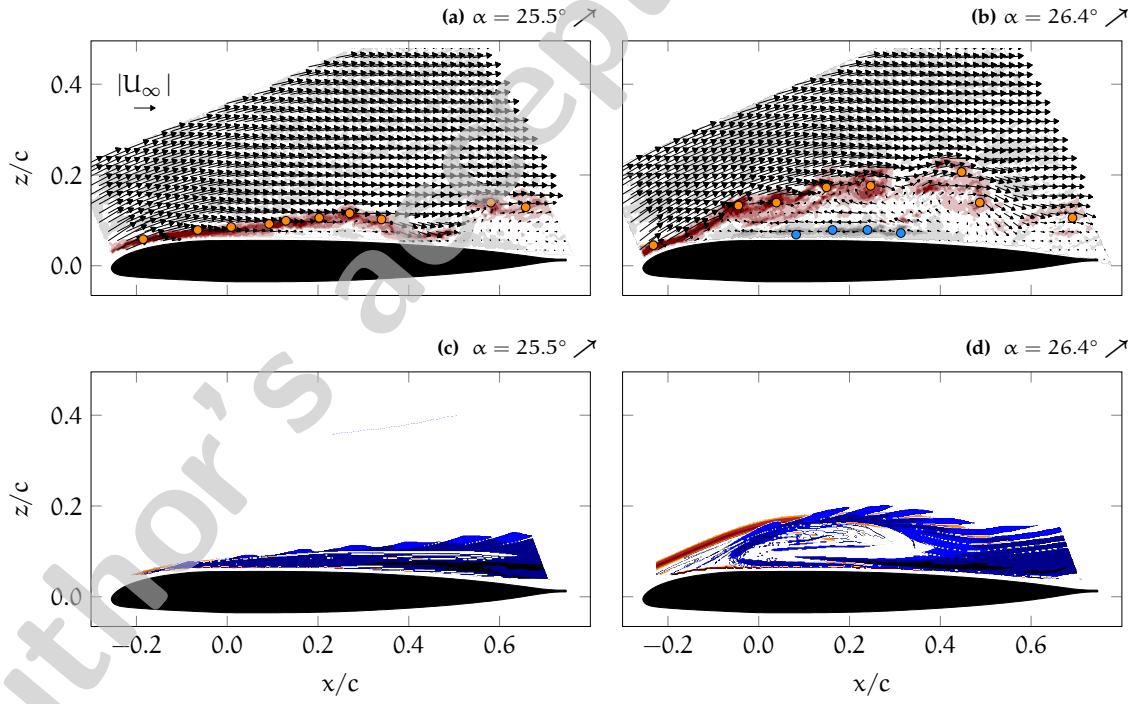

Figure 4: Difference of the flow topology and vortex distribution between the *primary instability* and the *vortex formation stage* ($\alpha = 25.5°$ and $26.4°$ on the upstroke ↗, respectively) indicated by: (a)-(b) the velocity field and the centres of (•) clockwise and (•) anticlockwise rotating vortices and (c)-(d) the corresponding Lagrangian coherent structures indicated by the ridges in the pFTLE and nFTLE fields ($\alpha_0 = 20°$, $\alpha_1 = 8°$, $k = 0.050$).

to model the airfoil's surface – induce an upstream velocity in their objects. In the region where a persistent adverse pressure gradient is present and the potential velocity no longer prevails the upward swimming velocity of the individual vortices, the vortex flow is able to move upstream. Due to the velocity difference with the outer flow a shear layer develops which is subsequently subjected to the primary instability. As a result of the latter the initial vorticity is redistributed in concentrated small-scale vortices.

Initially the shear layer vortices, all unidirectional-rotating, are more or less aligned and they interact only weakly with each other (figure 4(a)). The growth of the layer is approximately linear (cf. [2]) and the same is true for the increase of the mean height Δz. The linear fit describing the evolution of the shear layer height within the *primary instability stage* is indicated by a dashed line in figure 3(b). This linear relationship is valid until, at a later stage, the small shear layer vortices are subjected to the secondary instability and start to merge heralding shear layer roll up and the formation of the primary stall vortex. Simultaneously, counter-rotating vortices are induced near the airfoil profile as a result of strong interactions between the shear layer vortices and the reversed flow near the surface (figure 4(b)). During this stage the recirculation region grows swiftly and becomes of the order of the airfoil's thickness. The location and the size of the recirculation region within the two different stall development stages are indicated by the ridges in the pFTLE and nFTLE fields in figure 4(c)-(d). Furthermore, the rate of increase of Δz during the *vortex formation stage* is a measure for the rate of growth of the dynamic stall vortex.

The discontinuity in the temporal evolution of the shear layer height in figure 3(b) thus indicates a growing instability and marks the transition of the flow from the *primary instability* into the *vortex formation stage*. From an Eulerian point of view the transition point is defined by the intersection of the two linear fitting curves describing the rate of increase of Δz in the individual regimes. The time instant and angle of attack at which the transition takes place is denoted by t_{ds1} and α_{ds1}, respectively.

Additionally, from a Lagrangian point of view, the development of the secondary instability around $t = t_{ds1}$ is nicely observable in figure 5 representing a sequence of instantaneous LCSs. The depicted LCSs, identified by the ridges in the pFTLE and nFTLE fields, are extracted based on instantaneous velocity fields for subsequent time instants around $t = t_{ds1}$. The increasing bulgings of the ridges in the pFTLE and nFTLE fields readily indicate the growing instability of the shear layer leading to shear layer roll up. Consequently, the Lagrangian coherent structures analysis supports the conclusion that the passage from the first into the second stall development stage is triggered by a secondary instability of the shear layer.

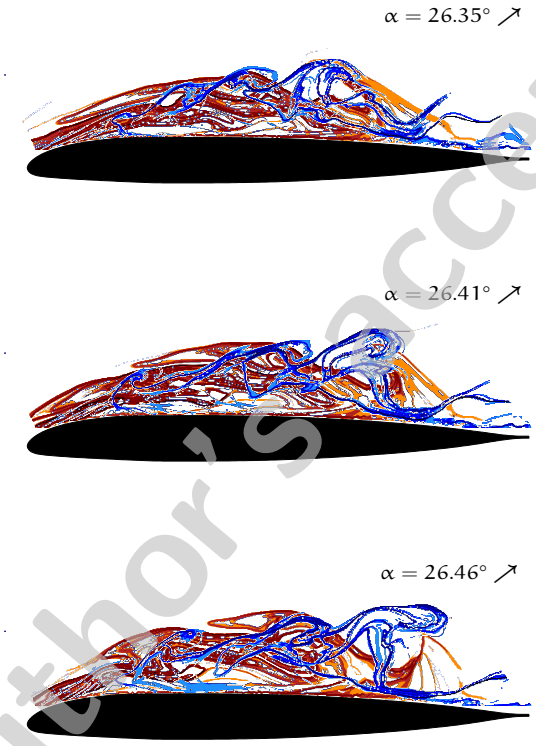

Figure 5: The pFTLE and nFTLE fields corresponding to consecutive time steps around the transition from the *primary instability* into the *vortex formation stage* ($\alpha_0 = 20°$, $\alpha_1 = 8°$, $k = 0.05$).

4.2 *Primary Instability Stage*

The question that remains is in what way the airfoil dynamics affect the formation and growth of the instability and therewith the dynamic stall vortex. Since the stall development stage has been divided into two parts characterised by a distinctly different behaviour of the shear layer it seems usefull, even necessary, to threat both stages individually.

The first part of the stall process is termed the *primary instability stage* and has been identified as the part of the dynamic stall life cycle that covers the initial development of a recirculation region on the airfoil's suction side and the formation of small-scale positive vortices at the interface as a result of a primary instability of the shear layer. The flow is conveniently considered quasi-static for angles of attack up to the static stall angle. Hence, the start of the *primary instability stage* is set at $t = t_{ss}$, i. e. the moment the angle of attack is increased

Table 1: Overview of the calculated dynamic stall quantities for different oscillation parameter combinations.

	k	α_0 [°]	α_1 [°]	α_{ds1} [°]	Δt_1 [s] $\times 10^{-2}$	α_{ds2} [°]	Δt_2 [s] $\times 10^{-3}$
△	0.050	18	6	23.97(5)	5.38(55)	24.04(1)	4(3)
○	0.100	18	6	23.65(12)	3.86(20)	23.94(8)	-
▲	0.050	18	8	25.35(10)	4.37(19)	25.75(5)	8(3)
●	0.100	18	8	25.94(6)	3.07(20)	25.81(6)	10(2)
△	0.050	20	6	24.97(9)	4.49(16)	25.53(11)	12(1)
□	0.075	20	6	25.60(6)	3.84(11)	25.99(2)	11(2)
○	0.100	20	6	25.83(10)	3.37(24)	25.89(6)	11(2)
▲	0.050	20	8	25.87(20)	3.92(22)	26.59(8)	8(1)
■	0.075	20	8	26.48(27)	3.03(23)	27.44(13)	9(3)
●	0.100	20	8	27.20(14)	2.83(13)	27.95(4)	9(2)
△	0.050	22	6	25.47(21)	4.36(27)	26.19(9)	9(3)
○	0.100	22	6	26.73(11)	3.04(9)	27.61(7)	9(1)
▲	0.050	22	8	26.01(13)	3.63(12)	27.06(6)	9(2)
●	0.100	22	8	27.94(19)	2.75(11)	29.03(16)	7(1)

The number in between the brackets is the standard deviation of the data.

beyond static stall. Its upper bound is given by t_{ds1}. The characteristic time delay attributed to the *primary instability stage* is denoted by Δt_1 and is calculated for all parameter combinations relevant to this study. The assessed values are listed in table 1.

Considering the behaviour of Δz in function of angle of attack, i. e. comparing α_{ds1} for the prevailing parameter combinations, yields the conclusion that the transition into the *vortex formation stage* is postponed to larger angles of attack with increasing frequency. However, comparing Δt_1 for the different degrees of unsteadiness reveals that the phase transition is actually promoted rather than delayed with increasing f_{osc} for constant mean incidence and oscillation amplitude. Regarding $\alpha 0$ and $\alpha 1$, their impact can not be investigated separately since they are interrelated parameters for the airfoil's motion and its derivatives.

The rate of change of the angle of attack[1], i. e. the first time derivative of $\alpha(t)$, is a measure for the instantaneous unsteadiness and is influenced by the oscillation frequency as well as by the mean incidence and the oscillation amplitude. The prevailing airfoil motion being sinusoidal, the rate of change of the angle of attack is inherently time-dependent, and moreover nonlinear.

Furthermore, the unsteady separation process comprises a series of events governed by much smaller time scales compared to the oscillation period. Hence, in order to outline the impact of the dynamic effects, an instantaneous effective measure for the unsteadiness should be considered rather than the reduced frequency which is only an overall measure. Since the role of the dynamic effects is generally considered minor up to the point where the angle of attack is increased beyond the static stall angle, the relevant instantaneous effective unsteadiness is determined here by the rate of change of α at $t = t_{ss}$, denoted by $\dot{\alpha}_{ss}$. In doing so the interrelated parameters i. e. mean incidence, amplitude, and oscillation frequency are gathered into a single parameter allowing for a more general investigation of the relation between unsteadiness and stall delay.

Presenting Δt_1 in function of the normalised effective unsteadiness $\dot{\alpha}_{ss}\, c/U_\infty$ in figure 6(a) reveals a monotonically decrease of the stall delay with increasing unsteadiness. Again a different picture emerges when regarding the dependence of the angle of attack α_{ds1} on the unsteadiness (figure 6(b)). Although the first part of the stall delay in terms α_{ds1} increases more or less nonlinearly with $\dot{\alpha}_{ss}\, c/U_\infty$ as predicted by Johnson and Ham [9], the incidence angle is considered not an adequate indicator for the unsteady processes and the actual time delay is preferred. Hence, it is suggested here that the unsteadiness speeds up the first part of the stall process rather than delaying it.

In figure 6 there seems to be one data point that is out of line with the others, namely the parameter combination $\alpha_0 = 18°$, $\alpha_1 = 6°$, and $k = 0.10$ depicted by the open gray circular symbol (○). This particular parameter combination yields a dynamic stall case that is also referred to as a *'light stall'* case. A light stall case can be recognised by the fact that the oscillation direction is changed before the dynamic stall onset angle is reached. Hence, massive flow separation is no

1 $\dot{\alpha}(t) = \frac{d\alpha(t)}{dt} = 2\pi f_{osc}\alpha_1 \cos(-\frac{\pi}{2} + 2\pi f_{osc} t)$.

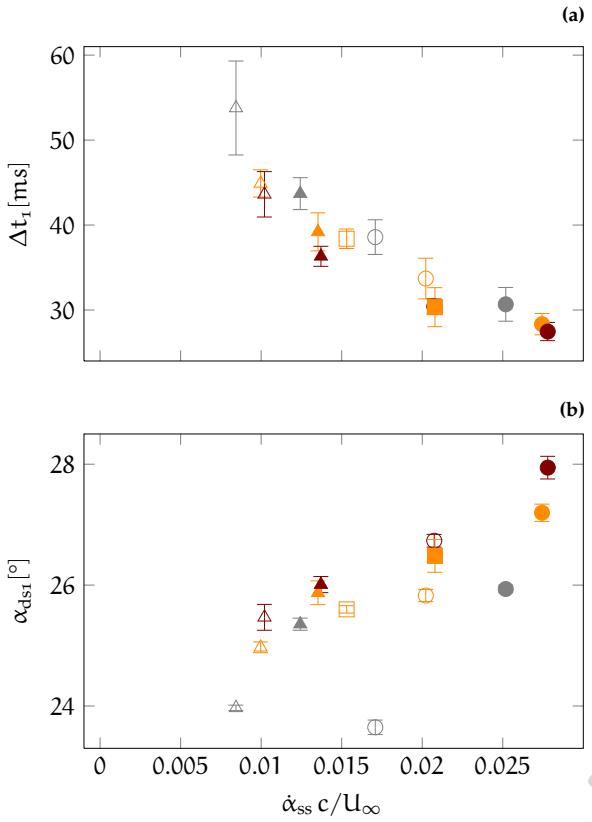

Figure 6: Influence of the rate of change of the angle of attack at $t = t_{ss}$ on (a) the stall delay Δt_1 and (b) the angle of incidence α_{ds1} for different oscillation parameter combinations indicated by different markers (cf. table 1). Error bars indicate the standard deviations.

longer initiated on the upstroke but is forced to occur on top of the cycle when less circulation is present. As a consequence, the height of the viscous zone enclosing separated flow is of the order of the airfoil thickness, and not of the order of the airfoil chord as for a deep stall case (cf. [12]).

4.3 *Vortex Formation Stage*

The second part of the stall development stage immediately following the *primary instability stage* is termed the *secondary instability* or the *vortex formation stage* and is characterised by the roll up of the shear layer into a large-scale dynamic stall vortex. The process leading to the formation of the primary stall vortex is identified as an instability of the shear layer that confines the reversing flow near the airfoil's surface.

Because a large portion of the overall vorticity is concentrated in the shear layer, the instability can also be seen as an instability of the vorticity distribution. Slight displacement of small vorticity packets and the generation of extra vorticity will alter the induced velocity for existing vortices and vortex lines, and consequentially change the vorticity pattern and the interactions between the viscous and inviscid parts of the flowfield. In particular, due to the altered process of production, convection and diffusion, the primarily small-scale shear layer vortices deviate from their initial trajectories, exert stronger mutual interactions and merge into larger coherent structures.

Furthermore, stronger interactions between the viscous-dominated shear layer and the reversed flow underneath it yield the emergence of counter-rotating vortices near the airfoil's surface. The presence of these negative vortices is indicated by the Eulerian picture (e. g. figure 4(b)). These vortices will play an essential role in the process leading to the dynamic stall onset. as they will be induced towards leading edge and lead to vortex induced separation

The dynamic stall onset angle of attack, defined previously from the experimental data based on a characteristic POD mode [14], is denoted by α_{ds2} and the time delay associated with the *vortex formation stage* is indicated by Δt_2. The assessed values of the onset angle of attack and the corresponding stall delay for the prevailing parameter combinations are also included in table 1.

The second contribution to the dynamic stall delay is found to be approximately constant for the presented parameter combinations (see also figure 7). Apparently, this part of the stall development is no longer influenced by dynamic effects, and the vortex formation process is solely governed by viscous interactions. Notice that for so-called *'light stall'* case given by the parameter combination $\alpha_0 = 18°$, $\alpha_1 = 6°$, and $k = 0.10$, there is no *vortex formation stage*, consequentially no Δt_2.

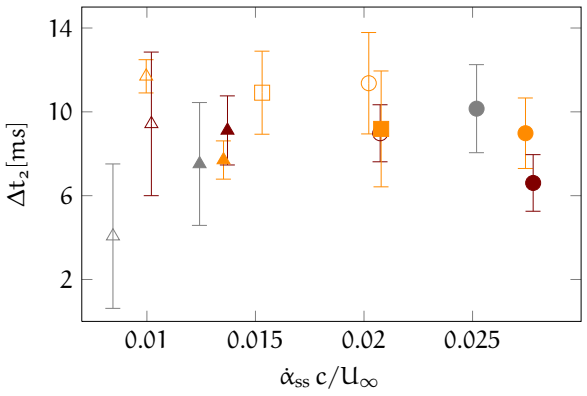

Figure 7: Dynamic stall delay attributed to the *vortex formation stage* for different oscillation parameter combinations indicated by different markers (cf. table 1). Error bars indicate the standard deviations.

5 CONCLUSION AND FUTURE WORK

Time-resolved velocity field information and unsteady surface pressure distributions were gathered during wind tunnel experiments and elaborated by an extensive coherent structure analysis. The characteristic features of the unsteady flow field were identified andanalysed utilising an Eulerian and a Lagrangian procedure that allow for the localisation of the axes of vortices and the edges of Lagrangian coherent structures, respectively. The complementary information obtained by both methods provided deeper insight into the spatiotemporal evolution of vortical structures within a single dynamic stall life cycle, and in particular within the stall development stage.

The classical hallmark of the dynamic stall phenomenon is the dynamic stall vortex. The physical mechanisms leading to the formation of this primary stall vortex were identified as the emergence and subsequent roll up of a local shear layer. Accordingly, the stall development stage was subdivided into two parts distinguished by their different dynamics: a primary instability stage followed by a secondary instability or vortex formation stage. During the former stage a recirculation region emerges on the airfoil's suction side as the result of a persisting unsteady adverse pressure gradient. At the interface between the reversed flow and the free stream flow small-scale shear layer vortices were identified by the Eulerian method. While observing only weak interactions during the first instability stage, the second stage was associated with the roll up of the shear layer into a large-scale dynamic stall vortex. The transition between the two stall development regimes was determined by a discontinuity in the development of the shear layer height. Furthermore, it was revealed that the dynamic stall delay attributed to the first instability stage decreases with increasing unsteadiness. The delay attributed to the vortex formation stage on the other hand was observed to be virtually unaffected by variations in the airfoil's pitching motion.

Due to the inherent unsteady nature of the dynamic stall process, the time-resolved approach has to be regarded the preferential approach. However, in order to further improve dynamic stall modelling and prediction, the parameter range should be extended, encompassing Reynolds number variations and alternative airfoil geometries.

Acknowledgements This work has been part of the DLR and ONERA joint project: Advanced Simulation and Control of Dynamic Stall (SIMCOS). The authors thank H. Mai, T. Büte, J. Nuhn and A. Henning for their contribution to the wind tunnel measurements.

REFERENCES

[1] L.W. Carr, K.W. McAlister, and W.J. McCroskey. Analysis of the development of dynamic stall based on oscillating airfoil experiments. TN D-8382, NASA, 1977.

[2] G.M. Corcos and F.S. Sherman. The mixing layer: Deterministic models of a turbulent flow. part 1. introduction and the two-dimensional flow. *J. Fluid Mech.*, 139:29–65, 1984.

[3] C. Garth, F. Gerhardt, X. Tricoche, and H. Hagen. Efficient computation and visualization of coherent structures in fluid flow applications. *IEEE Trans. Visual Comput. Graphics*, 13(6):1464–1471, November/December 2007.

[4] L. Graftieaux, M. Michard, and N. Grosjean. Combining PIV, POD and vortex identification algorithms for the study of unstready turbulent swirling flows. *Meas. Sci. Technol.*, 12:1422–1429, 2001.

[5] G. Haller. Lagrangian coherent structures from approximate velocity data. *Phys. Fluids*, 14(6):1851–1861, 2002.

[6] G. Haller. An objective definition of a vortex. *J. Fluid Mech.*, 525:1–26, 2005.

[7] G. Haller and G. Yuan. Lagragian coherent structures and mixing in two-dimensional turbulence. *Physica D*, 147:352–370, 2000.

[8] C.M. Ho. *Recent Advances in Aerodynamics*, chapter An Alternative Look at the Unsteady Separation Phenomenon, pages 165–178. Springer, 1986.

[9] W. Johnson and N.D. Ham. On the mechanism of dynamic stall. *AHS Journal*, 17(4):36–45, 1972.

[10] H.J. Lugt. *Recent Developments in Theoretical and Experimental Fluid Dynamics*, chapter The Dilemma of Defining a Vortex, pages 309–321. Springer, 1979.

[11] W.J. McCroskey. The phenomenon of dynamic stall. TM 81264, NASA, 1981.

[12] W.J. McCroskey and S.L. Pucci. Viscous-inviscid interactions on oscillating airfoils in subsonic flow. *AIAA J.*, 20(2):167–174, February 1982.

[13] M. Michard, L. Graftieaux, L. Lollini, and N. Grosjean. Identification of vortical structures by a non local criterion - application to PIV measurements and DNS-LES results of turbulent rotating flows. In *Proceedings of the* 11^{th} *Conference on Turbulent Shear Flows*, Grenoble, France, 1997.

[14] K. Mulleners and M. Raffel. A time-resolved dynamic stall investigation based on coherent structure analysis. In *Proceedings of the* 15^{th} *International Symposium on Applications of Laser Techniques to Fluid Mechanics*, Lisbon, Portugal, July 05–08 2010.

[15] A.V. Obabko and K.W. Cassel. Detachement of the dynamic stall vortex above a moving surface. *AIAA J.*, 40(9):1811–1822, September 2002.

[16] W.C. Reynolds and L.W. Carr. Review of unsteady, driven, separated flows. Paper 85-0527, AIAA, 1985.

[17] H. Richard, J. Bosbach, A. Henning, M. Raffel, and B.G. van der Wall. 2C and 3C PIV measurements on a rotor in hover condition. In *Proceedings of the* 13^{th} *International Symposium on Applications of Laser Techniques to Fluid Mechanics*, Lisbon, Portugal, June 26–29 2006.

[18] S.C. Shadden, F. Lekien, and J.E. Marsden. Definition and properties of Lagrangian coherent structures from finite-time lyapunov exponents in two-dimensional aperiodic flows. *Physica D*, 212:271–304, 2005.

[19] C. Shih, L. Lourenco, L. Van Dommelen, and A. Krothapalli. Unsteady flow past an airfoil pitching at constant rate. *AIAA J.*, 30(5):1153–1161, May 1992.

[20] A. Spentzos, G. Barakos, K. Badcock, B. Richard, P. Werner, S. Schreck, and M. Raffel. Investigation of three-dimensional dynamic stall using computational fluid dynamics. *AIAA J.*, 43(5):1023–1033, 2005.

[21] P. Wernert, W. Geissler, M. Raffel, and J. Kompenhans. Experimental and numerical investigations of dynamic stall on a pitching airfoil. *AIAA J.*, 34 (5):982–989, 1996.